



DIGITAL
LIBRARY

dspace.vutbr.cz

Imaging of near-field interference patterns by aperture-type SNOM – influence of illumination wavelength and polarization state

DVOŘÁK, P.; ÉDES, Z.; KVAPIL, M.; ŠAMOŘIL, T.; LIGMAJER, F.; HRTOŇ, M.; KALOUSEK, R.; KRÁPEK, V.; DUB, P.; SPOUSTA, J.; VARGA, P.; ŠIKOLA, T.

Citation: Opt. Express 25, 16560-16573 (2017)

ISSN: 1094-4087

DOI: <https://doi.org/10.1364/OE.25.016560>

Final PDF version



Imaging of near-field interference patterns by aperture-type SNOM – influence of illumination wavelength and polarization state

PETR DVOŘÁK,^{1,2,*} ZOLTÁN ÉDES,^{1,2} MICHAL KVAPIL,^{1,2} TOMÁŠ ŠAMOŘIL,^{1,2} FILIP LIGMAJER,^{1,2} MARTIN HRTOŇ,^{1,2} RADEK KALOUSEK,^{1,2} VLASTIMIL KŘÁPEK,^{1,2} PETR DUB,^{1,2} JIŘÍ SPOUSTA,^{1,2} PETER VARGA,² AND TOMÁŠ ŠIKOLA^{1,2}

¹Institute of Physical Engineering, Brno University of Technology, Technická 2896/2, 616 69 Brno, Czech Republic

²Central European Institute of Technology, Purkyňova 123, 612 00 Brno, Czech Republic

*petr.dvorak@ceitec.vutbr.cz

Abstract: Scanning near-field optical microscopy (SNOM) in combination with interference structures is a powerful tool for imaging and analysis of surface plasmon polaritons (SPPs). However, the correct interpretation of SNOM images requires profound understanding of principles behind their formation. To study fundamental principles of SNOM imaging in detail, we performed spectroscopic measurements by an aperture-type SNOM setup equipped with a supercontinuum laser and a polarizer, which gave us all the degrees of freedom necessary for our investigation. The series of wavelength- and polarization-resolved measurements, together with results of numerical simulations, then allowed us to identify the role of individual near-field components in formation of SNOM images, and to show that the out-of-plane component generally dominates within a broad range of parameters explored in our study. Our results challenge the widespread notion that this component does not couple to the aperture-type SNOM probe and indicate that the issue of SNOM probe sensitivity towards the in-plane and out-of-plane near-field components – one of the most challenging tasks of near field interference SNOM measurements – is not yet fully resolved.

© 2017 Optical Society of America

OCIS codes: (250.5403) Plasmonics; (130.1750) Components; (300.0300) Spectroscopy; (100.3175) Interferometric imaging.

References and links

1. W. D. Pohl, *Near-Field Optics and Surface Plasmon Polaritons* (Springer, 2001).
2. W. D. Pohl, W. Denk, and M. Lanz, “Optical stethoscopy: Image recording with resolution $\lambda/20$,” *Appl. Phys. Lett.* **44**(7), 651–653 (1984).
3. L. Novotny and B. Hecht, *Principles of Nano-Optics*, 2nd ed. (Cambridge University, 2012).
4. M. Schnell, P. Sarriugarte, T. Neuman, A. B. Khanikaev, G. Shvets, J. Aizpurua, and R. Hillenbrand, “Real-Space Mapping of the Chiral Near-Field Distributions in Spiral Antennas and Planar Metasurfaces,” *Nano Lett.* **16**(1), 663–670 (2016).
5. R. Hillenbrand, “Towards phonon photonics: scattering-type near-field optical microscopy reveals phonon-enhanced near-field interaction,” *Ultramicroscopy* **100**(3-4), 421–427 (2004).
6. B. J. Bohn, M. Schnell, M. A. Kats, F. Aieta, R. Hillenbrand, and F. Capasso, “Near-Field Imaging of Phased Array Metasurfaces,” *Nano Lett.* **15**(6), 3851–3858 (2015).
7. B. Hecht, B. Sick, U. P. Wild, V. Deckert, R. Zenobi, O. J. F. Martin, and D. W. Pohl, “Scanning near-field optical microscopy with aperture probes: Fundamentals and applications,” *J. Chem. Phys.* **112**(18), 7761–7774 (2000).
8. B. N. Tugchin, N. Janunts, A. E. Klein, M. Steinert, S. Fasold, S. Diziain, M. Sison, E.-B. Kley, A. Tünnermann, and T. Pertsch, “Plasmonic Tip Based on Excitation of Radially Polarized Conical Surface Plasmon Polariton for Detecting Longitudinal and Transversal Fields,” *ACS Photonics* **2**(10), 1468–1475 (2015).
9. P. Dvořák, T. Neuman, L. Břínek, T. Šamořil, R. Kalousek, P. Dub, P. Varga, and T. Šikola, “Control and near-field detection of surface plasmon interference patterns,” *Nano Lett.* **13**(6), 2558–2563 (2013).

10. W. L. Barnes, A. Dereux, and T. W. Ebbesen, "Surface plasmon subwavelength optics," *Nature* **424**(6950), 824–830 (2003).
11. M. C. Quong and A. Y. Elezzabi, "Selective optical-optical switching for planar plasmonic waveguides and nodes," *Opt. Express* **16**(11), 8198–8212 (2008).
12. N. Yu and F. Capasso, "Flat optics with designer metasurfaces," *Nat. Mater.* **13**(2), 139–150 (2014).
13. Z. W. Liu, Q. H. Wei, and X. Zhang, "Surface plasmon interference nanolithography," *Nano Lett.* **5**(5), 957–961 (2005).
14. Z. Xie, W. Yu, T. Wang, H. Zhang, Y. Fu, H. Liu, F. Li, Z. Lu, and Q. Sun, "Plasmonic Nanolithography: A Review," *Plasmonics* **6**(3), 565–580 (2011).
15. M. L. Juan, M. Righini, and R. Quidant, "Plasmon nano-optical tweezers," *Nat. Photonics* **5**(6), 349–356 (2011).
16. J. N. Anker, W. P. Hall, O. Lyandres, N. C. Shah, J. Zhao, and R. P. Van Duyne, "Biosensing with plasmonic nanosensors," *Nat. Mater.* **7**(6), 442–453 (2008).
17. C. Valsecchi and A. G. Brolo, "Periodic metallic nanostructures as plasmonic chemical sensors," *Langmuir* **29**(19), 5638–5649 (2013).
18. S. Zeng, D. Baillargeat, H.-P. Ho, and K.-T. Yong, "Nanomaterials enhanced surface plasmon resonance for biological and chemical sensing applications," *Chem. Soc. Rev.* **43**(10), 3426–3452 (2014).
19. L. Guo, Y. Huang, Y. Kikutani, Y. Tanaka, T. Kitamori, and D.-H. Kim, "In situ assembly, regeneration and plasmonic immunosensing of a Au nanorod monolayer in a closed-surface flow channel," *Lab Chip* **11**(19), 3299–3304 (2011).
20. Y. Gao, Z. Xin, B. Zeng, Q. Gan, X. Cheng, and F. J. Bartoli, "Plasmonic interferometric sensor arrays for high-performance label-free biomolecular detection," *Lab Chip* **13**(24), 4755–4764 (2013).
21. G. Obara, N. Maeda, T. Miyanishi, M. Terakawa, N. N. Nedyalkov, and M. Obara, "Plasmonic and Mie scattering control of far-field interference for regular ripple formation on various material substrates," *Opt. Express* **19**(20), 19093–19103 (2011).
22. J. Lin, J. P. B. Mueller, Q. Wang, G. Yuan, N. Antoniou, X.-C. Yuan, and F. Capasso, "Polarization-controlled tunable directional coupling of surface plasmon polaritons," *Science* **340**(6130), 331–334 (2013).
23. A. E. Klein, N. Janunts, M. Steinert, A. Tünnermann, and T. Pertsch, "Polarization-resolved near-field mapping of plasmonic aperture emission by a dual-SNOM system," *Nano Lett.* **14**(9), 5010–5015 (2014).
24. J. Chen, M. Badioli, P. Alonso-González, S. Thongrattanasiri, F. Huth, J. Osmond, M. Spasenović, A. Centeno, A. Pesquera, P. Godignon, A. Z. Elorza, N. Camara, F. J. García de Abajo, R. Hillenbrand, and F. H. L. Koppens, "Optical nano-imaging of gate-tunable graphene plasmons," *Nature* **487**(7405), 77–81 (2012).
25. X. Zeng, H. Hu, Y. Gao, D. Ji, N. Zhang, H. Song, K. Liu, S. Jiang, and Q. Gan, "Phase change dispersion of plasmonic nano-objects," *Sci. Rep.* **5**(1), 12665 (2015).
26. M. Burresi, D. van Oosten, T. Kampfrath, H. Schoenmaker, R. Heideman, A. Leinse, and L. Kuipers, "Probing the magnetic field of light at optical frequencies," *Science* **326**(5952), 550–553 (2009).
27. H. W. Kihm, S. M. Koo, Q. H. Kim, K. Bao, J. E. Kihm, W. S. Bak, S. H. Eah, C. Lienau, H. Kim, P. Nordlander, N. J. Halas, N. K. Park, and D.-S. Kim, "Bethe-hole polarization analyser for the magnetic vector of light," *Nat. Commun.* **2**, 451 (2011).
28. H. W. Kihm, J. Kim, S. Koo, J. Ahn, K. Ahn, K. Lee, N. Park, and D.-S. Kim, "Optical magnetic field mapping using a subwavelength aperture," *Opt. Express* **21**(5), 5625–5633 (2013).
29. B. le Feber, N. Rotenberg, D. M. Beggs, and L. Kuipers, "Simultaneous measurement of nanoscale electric and magnetic optical fields," *Nat. Photonics* **8**(1), 43–46 (2013).
30. N. Rotenberg and L. Kuipers, "Mapping nanoscale light fields," *Nat. Photonics* **8**(12), 919–926 (2014).
31. M. Urbánek, V. Uhlíř, P. Bábor, E. Kolíbalová, T. Hrnčíř, J. Spousta, and T. Šíkola, "Focused ion beam fabrication of spintronic nanostructures: an optimization of the milling process," *Nanotechnology* **21**(14), 145304 (2010).
32. P. B. Johnson and R. W. Christy, "Optical Constants of the Noble Metals," *Phys. Rev. B* **6**(12), 4370–4379 (1972).
33. R. L. Olmon, B. Slovick, T. W. Johnson, D. Shelton, S.-H. H. Oh, G. D. Boreman, and M. B. Raschke, "Optical dielectric function of gold," *Phys. Rev. B* **86**(23), 235147 (2012).
34. T. Šíkola, J. Spousta, L. Ditrichová, L. Beneš, V. Peřina, and D. Rafaja, "Ion beam assisted deposition of metallic and ceramic thin films," *Nucl. Instrum. Methods Phys. Res. B* **127**(127–128), 673–676 (1997).
35. U. Schröter and D. Heitmann, "Surface-plasmon-enhanced transmission through metallic gratings," *Phys. Rev. B* **58**(23), 15419–15421 (1998).
36. M. Mansuripur, X. Yong, A. R. Zakharian, and J. V. Moloney, "Transmission of light through slit apertures in metallic films," *IEEE Trans. Magn.* **41**(2), 1012–1015 (2005).
37. H. F. Schouten, N. Kuzmin, G. Dubois, T. D. Visser, G. Gbur, P. F. A. Alkemade, H. Blok, G. W. Hooft, D. Lenstra, and E. R. Eliel, "Plasmon-assisted two-slit transmission: Young's experiment revisited," *Phys. Rev. Lett.* **94**(5), 053901 (2005).
38. S. A. Maier, *Plasmonics: Fundamentals and Applications* (Springer US, 2007).
39. L. Aigouy, P. Lalanne, J. P. Hugonin, G. Julié, V. Mathet, and M. Mortier, "Near-field analysis of surface waves launched at nanoslit apertures," *Phys. Rev. Lett.* **98**(15), 153902 (2007).
40. M. Hentschel, T. Weiss, S. Bagheri, and H. Giessen, "Babinet to the half: coupling of solid and inverse plasmonic structures," *Nano Lett.* **13**(9), 4428–4433 (2013).

41. Q. Wang, J. Bu, and X.-C. Yuan, "High-resolution 2D plasmonic fan-out realized by subwavelength slit arrays," *Opt. Express* **18**(3), 2662–2667 (2010).
42. E. A. Bezuš, A. A. Morozov, B. O. Volodkin, K. N. Tukmakov, S. V. Alferov, and L. L. Doskolovich, "Formation of high-frequency two-dimensional interference patterns of surface plasmon polaritons," *JETP Lett.* **98**(6), 317–320 (2013).
43. X. Li, Y. Gao, S. Jiang, L. Ma, C. Liu, and C. Cheng, "Experimental solution for scattered imaging of the interference of plasmonic and photonic mode waves launched by metal nano-slits," *Opt. Express* **23**(3), 3507–3522 (2015).
44. M. Esslinger and R. Vogelgesang, "Reciprocity theory of apertureless scanning near-field optical microscopy with point-dipole probes," *ACS Nano* **6**(9), 8173–8182 (2012).
45. S. Schmidt, A. E. Klein, T. Paul, H. Gross, S. Diziaín, M. Steinert, A. C. Assafrao, T. Pertsch, H. P. Urbach, and C. Rockstuhl, "Image formation properties and inverse imaging problem in aperture based scanning near field optical microscopy," *Opt. Express* **24**(4), 4128–4142 (2016).
46. M. Burresi, R. J. P. Engelen, A. Opheij, D. van Oosten, D. Mori, T. Baba, and L. Kuipers, "Observation of polarization singularities at the nanoscale," *Phys. Rev. Lett.* **102**(3), 033902 (2009).
47. A. Minovich, A. E. Klein, N. Janunts, T. Pertsch, D. N. Neshev, and Y. S. Kivshar, "Generation and near-field imaging of Airy surface plasmons," *Phys. Rev. Lett.* **107**(11), 116802 (2011).
48. D. Denkova, N. Verellen, A. V. Silhanek, V. K. Valev, P. Van Dorpe, and V. V. Moshchalkov, "Mapping magnetic near-field distributions of plasmonic nanoantennas," *ACS Nano* **7**(4), 3168–3176 (2013).
49. P. Ginzburg, E. Hirshberg, and M. Orenstein, "Rigorous analysis of vectorial plasmonic diffraction: single- and double-slit experiments," *J. Opt. A, Pure Appl. Opt.* **11**(11), 114024 (2009).
50. P. Lalanne, J. P. Hugonin, and J. C. Rodier, "Theory of surface plasmon generation at nanoslit apertures," *Phys. Rev. Lett.* **95**(26), 263902 (2005).

1. Introduction

Scanning near-field optical microscopy (SNOM) has become a powerful instrument for experimental studies of optical near-fields [1–4]. Depending on the spectral region of the detected field, different types of SNOM probes are preferred. For detection in the infrared (IR), the most suitable technique is so called s-SNOM, which is based on scattering from an apertureless SNOM tip [5,6]. On the other hand, in the visible, a SNOM tip with aperture is frequently used and the technique is known as a-SNOM [3,7,8]. The a-SNOM probe consists of an optical fiber etched at its end into a tip covered by a metal coating with a small aperture at its apex. This probe is approached in a controlled way (using a non-contact mode of an atomic force microscope, AFM) to a sample surface where it couples with the near field. Although the tip partially distorts the distribution of the near-field, the detected optical signal principally reflects the original field distribution, as shown for instance in our previous work [9].

As surface plasmon polaritons (SPPs) are inherently connected to near-fields, they are a frequent object of study by SNOM – both in their localized (to metal nanoobjects) and propagating (along metal-dielectric interfaces) form [10]. A special class of SPP that lies in between those two categories is represented by patterns of SPP standing waves. These can arise on plasmonic interference structures, formed e.g. by pairs of slits in a continuous metal film, which act as linear sources of SPP when illuminated by light. Standing waves in resulting interference patterns have found applications in 2D optics [11,12], nanolithography [13,14], manipulation with nanoobjects [15], and bio- and chemical sensing [16–20].

The interference patterns can be controlled via geometry of slits, refractive index of environment, or apparently by optical parameters of illumination, i.e. wavelength, phase, and polarization [21–23]. Control of the patterns by these optical parameters has not been widely used yet, most likely due to associated technical complications. For instance, to our best knowledge, a-SNOM detection of SPP interference patterns has been done only in a monochromatic mode so far, i.e. just at one or a few selected wavelengths [24,25]. Besides, it was recently shown that also the magnetic components can strongly contribute to the detected SNOM signal in some specific situations [26–29]. It is evident that for the correct interpretation of acquired near field images, the understanding of principles behind the formation of interference patterns and the role of individual electric/magnetic, in-plane/out-of-plane near-field components [Fig. 1(a)] is fundamental [30]. In our previous paper [9], we

have briefly discussed this subject for a limited case of polarized monochromatic light, yet a systematic and detailed analysis of these aspects has been missing. To tackle this issue, we have performed spectroscopic measurements by our a-SNOM setup for both polarized and unpolarized illumination light generated by a supercontinuum laser (see Fig. 2) for more details of experimental setup). In this way, a bigger variety of interference patterns has been obtained and thus more general study could be performed. Together with numerical finite-difference time-domain (FDTD) simulations, our experimental results provide a comprehensive description of SNOM image formation. Such knowledge can be utilized in determination of SNOM probe sensitivity towards individual near-field components, which still remains a challenge in SNOM experiments.

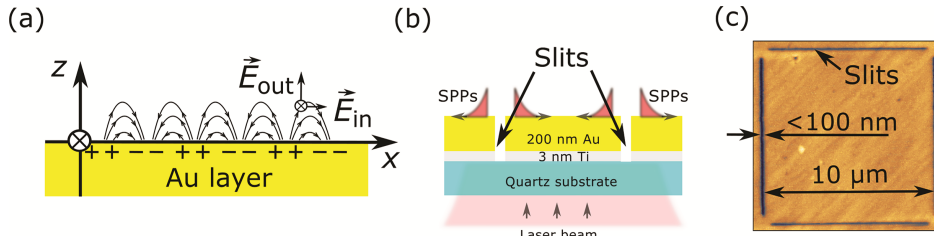


Fig. 1. (a) Schematic of a SPP wave propagating along the metal-air interface with the marked near-field vectors. (b) Schematic of the sample cross-section with the slits carved into the metal layers using FIB. Note that the laser beam is not drawn in scale. (c) AFM topography image of the interference structure.

For measuring the distribution of near-field intensity of SPP interference patterns a SNOM microscope schematically shown in Fig. 2 was used. A supercontinuum laser (Fianium) with tunable laser wavelengths and maximum output power of 6 mW/nm (in the visible) was connected to a commercial SNOM instrument (NT-MDT Ntegra Solaris). The laser beam was guided through an inverted microscope (Olympus IX71) and focused on the sample with a $60 \times$ objective ($NA = 0.7$). A linear polarizer was placed in front of the objective to control the polarization of the incoming light. The homogeneity of illumination of all four slits was achieved by the following procedure: First, the laser beam was focused as tightly as possible (spot size $\approx 2 \mu\text{m}$) and aligned with the center of the interference structure. Then, the intensity of light transmitted through the individual slits in two perpendicular SNOM line scans was monitored and made equal by further sample micro-positioning (within margin of error of $\approx 5\%$). Finally, the perfectly centered beam was defocused up to the spot size of $\approx 30 \mu\text{m}$, which assured homogeneous illumination on the scale much larger than the dimensions of our interference structures. The optical signal was collected through an aperture of an in-house developed probe and guided into a photodetector. The diameter of the aperture was $\sim 50 \text{ nm}$ and the thickness of the metallic coating was $\sim 130 \text{ nm}$.

2. Results and discussion

Samples with interference structures consisting of four slits in square arrangement were prepared by carving out a 200 nm-thick gold film on a glass substrate using Ga focused-ion-beam (FIB) milling [Fig. 1(b) and 1(c)] [31]. The thickness of the gold layer was set large enough to avoid penetration of light from the illumination source through it. Gold was chosen as a material which has plasma frequency in the optical range, can be easily etched, and is resistive to oxidation [32,33]. To increase adhesion of the gold film to the glass, a 3 nm-thick titanium layer was used. The fabricated slits were no more than 100 nm wide and thus well below the diffraction limit for the visible light. Both metal layers were deposited using ion-beam-sputtering deposition with a beam energy of 600 eV [34]. The FIB energy was set to 30 keV and the spot size was $\sim 30 \text{ nm}$. To avoid charging effects in the area inside the slits during the milling process, the slits were not fully interconnected. The excitation of

SPPs occurs at the fabricated slits via the electromagnetic wave incident on the interference structure from the bottom [35–37]. SPPs then propagate along the metal-air interface in directions perpendicular to the slits, with the wavelength (λ_{SPP}) proportional to the illumination one (λ_0) [38,39]. The resulting electromagnetic field can be simply modeled analytically: By summation of radiation from dipoles distributed equidistantly along the slit [9], or via interference of SPPs propagating along the surface in the perpendicular direction away from the slits. Apparently, the efficiency of the SPP excitation depends on the polarization of the incoming light and it reaches its maximum when the polarization vector is perpendicular to a slit[40].

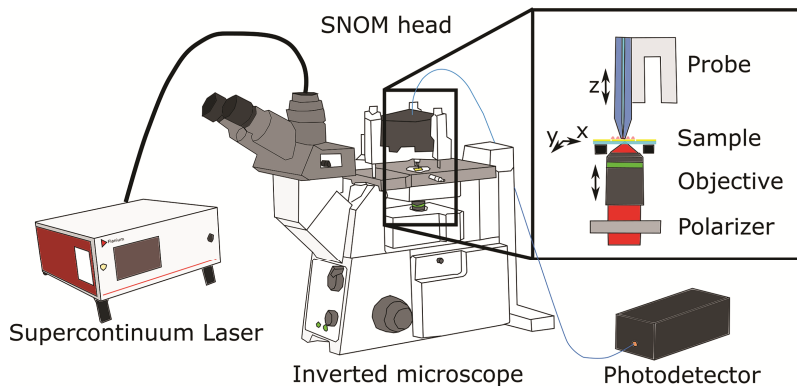


Fig. 2. Schematic of the SNOM microscope with the supercontinuum laser light source. The inverted microscope enables to focus the light beam to an interference structure and set its polarization. The optical signal is detected via the home-made SNOM probe and guided by the optical fiber into the photodetector.

To accurately describe the resulting SPP interference patterns (5 nm above the surface) without the presence of a SNOM probe, we performed FDTD simulations (Lumerical FDTD Solutions 7.5.5) for monochromatic light polarized along the diagonal of the slit structure that was later studied experimentally [9]. In Figs. 3(a) and 3(b) we show that the simulated interference pattern changes from a diamond-like to a square-like one, depending on whether the out-of-plane (E_{out}) or the in-plane (E_{in}) component of the electric field, respectively, is taken into account. Existence of these two forms of patterns stems from the interference of two standing SPP waves located between orthogonal pairs of slits (see Fig. 4). Note that our numerical simulations showed that the magnetic field forms patterns identical to those above. Thus on one hand, our structures cannot be used for the study of relative sensitivity towards electric and magnetic fields [28], but on the other hand, eventual detection of the magnetic fields will have no influence on the observed patterns and on our conclusions derived from them. Moreover, as the SPPs at gold-air interface are transverse magnetic waves, their out-of-plane component of magnetic field is negligible and we can leave it out of our analysis.

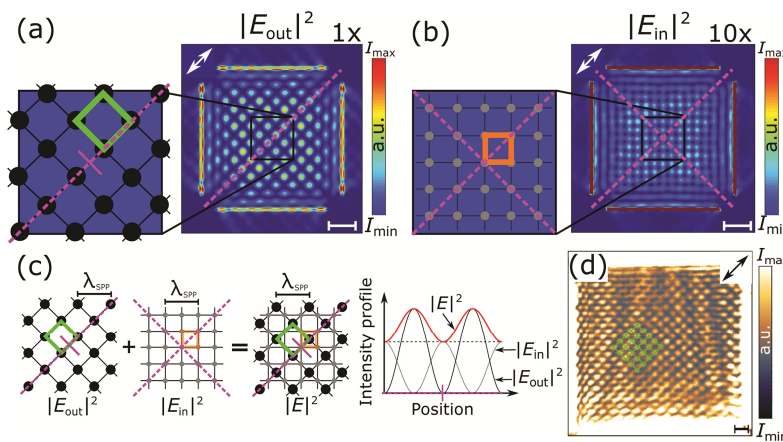


Fig. 3. Interference patterns of the square of modulus of (a) out-of-plane and (b) in-plane electric field components calculated for linearly polarized illumination (polarization direction marked by the white double arrows) at $\lambda = 632$ nm. Note that the dimensions of the interference structures were only $(5 \times 5) \mu\text{m}^2$ for better visualization and the $|E_{in}|^2$ values in (b) are multiplied by a factor of 10. The purple dashed lines represent the symmetry axes. The zoomed images show a schematic of the central region of the interference patterns with the colored squares indicating their character. (c) Schematic of individual interference patterns of the E_{in} and E_{out} components and their superposition together with the intensity profile along the axis of symmetry. Note that the bright spots (maxima) of both patterns do not overlap. (d) Experimental interference pattern for linearly polarized light ($\lambda = 632$ nm). All scale bars are $1 \mu\text{m}$.

As the detected SNOM image is expected to reproduce the SPP fields, it should also be a superposition of the two types of patterns described above. Yet in our experiment (Fig. 3(d)), we observed only a distinct diamond-like pattern. This is consistent with the fact that intensity of the out-of-plane electric component is more than ten times higher [compare the scale bars in Figs. 3(a) and 3(b)] and in line with some similar experiments reported in the past [9,41–43]. These results are, however, in contradiction with a widespread notion that the out-of-plane component cannot be detected by the a-SNOM probe. This assertion is based on the supposed incompatibility of the SPP out-of-plane components with the “guided” modes of the aperture that emerged from theoretical considerations [27,29,44,45] and has been supported by several experimental works [46–48]. This contradictory evidence renders any categorical statement about the inability to detect one or the other component questionable. To fully address this controversial issue, we first need to discuss absolute positions of the diamond- and square-like patterns.

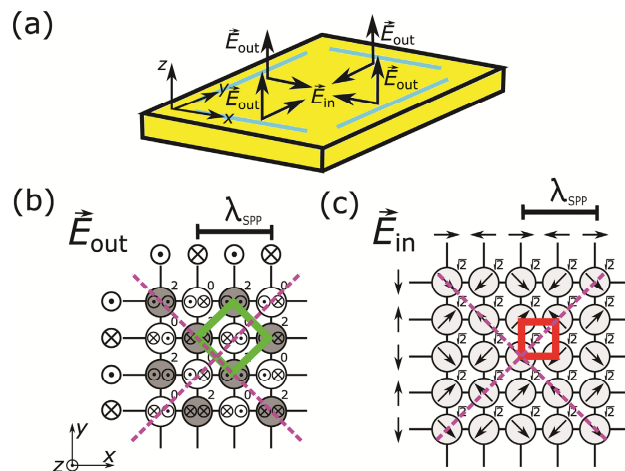


Fig. 4. (a) Schematic of the formation of SPP interference patterns at the 4-slit structure for illumination polarized in the direction perpendicular to the diagonal of the structure. (b) Creation of the diamond-like interference pattern by the superposition of the SPP out-of-plane components. The resulting pattern motif is marked by a green diamond. (c) Creation of the square-like interference pattern (red square) by the superposition of the SPP in-plane components. The arrows in (b) and (c) depict the electric field orientation and the resulting amplitudes are indicated numerically for each grid point. The corresponding SPP wavelength is indicated by the bar at the top of the schemes.

In Fig. 3(c), we schematically depict distributions of pattern maxima extracted from the simulations in Figs. 3(a) and 3(b) (with respect to the center of symmetry of the whole interference structure). It is clear that the E_{in} and E_{out} patterns differ not only in their shape but also in their absolute position. This is an important result for SNOM, as it makes this class of interference structures a useful platform for assessing the SNOM sensitivity towards the individual near-field components. In particular, by comparing the measured and calculated intensity profiles along the symmetry axis containing intensity maxima, the relative weight of detected components could be estimated (with the uncertainty given by the possible contribution of the in-plane magnetic field to the detected signal, as stated above). The experimental verification, however, requires measurements with high resolution, low signal-to-noise ratio, and calibration (due to possible non-zero background) that we were unable to carry out using our current experimental setup. Nevertheless, we decided to draw on this idea in theoretical simulations of the a-SNOM detection process, with the aim to elucidate the presence of the out-of-plane component in our measurements. To this end we incorporated a model of a SNOM probe into the existing simulations of SPP patterns [see Fig. 5(a)] and analyzed the power transmitted into the dielectric core of the optical fiber for different positions of the probe along a diagonal of the SPP interference pattern. The results of these simulations, plotted in Fig. 5(b), clearly show a spatial profile that very well matches the distribution of the out-of-plane component extracted from the SPP interference pattern calculated for the bare interference structure, i.e. without the presence of the SNOM probe. The fact that the out-of-plane field indeed couples to the perfectly symmetric probe is an important finding that supports our claims and, interestingly, is in contrast with previous studies. Simultaneously, it is worth noting that the power detected close to the apex of the probe may not exactly match the signal at the detector. However, the analysis of the whole signal path, i.e. from the tip apex through the guided modes of the optical fiber to the detector, is beyond the scope of this work. At this point, one might also consider the possibility that the strong sensitivity towards the out-of-plane component is caused by a tilt of the tip with respect to the sample: For the out-of-plane component to be detectable, its in-plane projection into the tip-coordinate frame would need to be at least comparable to the

corresponding projection of the in-plane component. This would, however, require a tilt exceeding 10 degrees, which is definitely not the case in our setup. So based on these simple geometrical considerations, we may rule out the tilt of the tip as the cause of the probe sensitivity towards the out-of-plane component. Therefore, we believe that both the simulations and the experiments presented here constitute a compelling evidence that the out-of-plane component can efficiently couple to the probe and strongly contribute to the signal detected by a-SNOM in certain situations. The suspected mechanism facilitating this coupling is a leakage of the probed field through the tip sidewalls [8]. Moreover, our numerical simulations suggest that aperture shape and dimensions also strongly affect the type of the detected signal [see Fig. 5(b)]. We therefore hypothesize that the large variety of aperture diameters and coating thicknesses encountered in previously published works could be the source of the contradictory statements regarding the SNOM sensitivity.

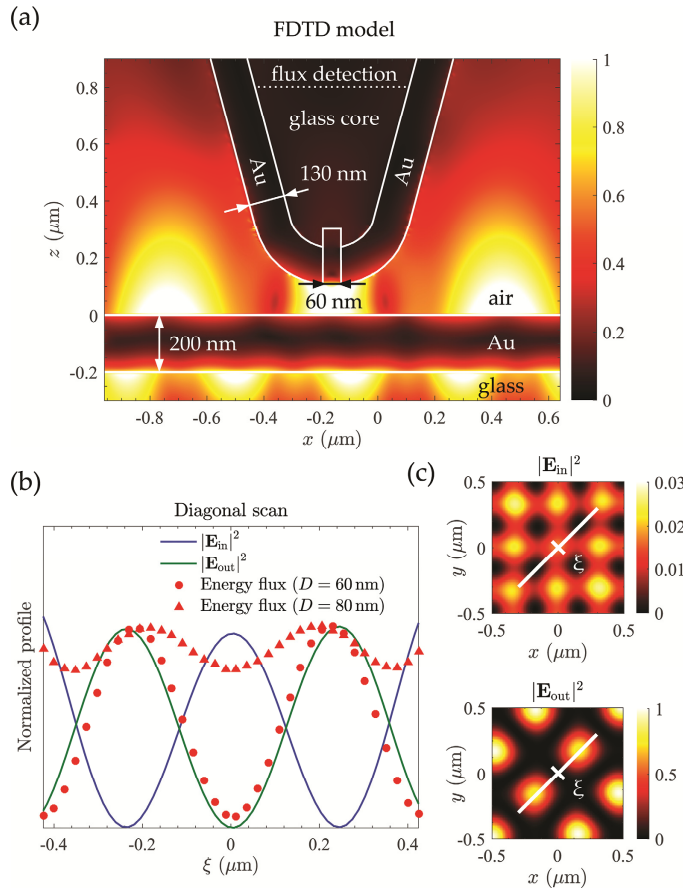


Fig. 5. FDTD calculations of SPP interference patterns (illumination wavelength $\lambda_0 = 650$ nm) with a SNOM probe implemented into the model. (a) Amplitude of the electric field in the vicinity of a SNOM probe with the shape and size matching the one used in experiments. (b) The power transmitted through the aperture into the glass core calculated by integrating the Poynting vector over its cross-section 700 nm above the tip apex. Red circles and triangles show this transmitted power as a function of the tip position ξ along the diagonal of the SPP interference pattern for aperture with diameter 60 nm (same as in our experiments) and 80 nm, respectively. The resulting (discrete) ξ -profiles are overlaid with the profiles of SPP near-field components (blue and green line) extracted from simulations without the SNOM probe shown in (c). The energy flux through the smaller aperture corresponds to the out-of-plane component, whereas the flux through the larger one exhibits a mixed character with contribution from both components. Note that each point in (b) corresponds to one simulation and one position of the probe along the diagonal indicated by the white line in (c).

Now that we have dealt with the central aspects of our system, we turn our attention towards scenario with unpolarized monochromatic ($\lambda = 650$ nm) illumination. In contrast with the previous measurements involving polarized light, we observed a square-like pattern [Fig. 6(a)] with periodicity corresponding only to the half of the calculated SPP wavelength λ_{SPP} (the periodicity was obtained from the image analysis using the Fast Fourier Transform (FFT) method). These experimental results were supported by FDTD simulations [Fig. 6(b)], which confirmed both the pattern shape and its periodicity. The simulations also provided quantitative information about the pattern intensity, which turned out to be lower by one half than for the polarized illumination. To explain these results, it is necessary to recall that any unpolarized light can be naturally broken down into two perpendicularly-polarized components. These two components will excite two orthogonal diamond-like interference patterns which will add up incoherently, i.e. the square of the modulus of their electric and magnetic fields will be summed up [Fig. 6(c)]. But owing to their mutual shift, the regions of maximum intensity of one pattern will be located in the regions of minimum intensity of the other one. In this way, the square-like pattern is formed with halved periodicity and doubled degree of rotational symmetry compared to the patterns arising from polarized illumination. Note that in the above interpretation we do not consider the in-plane pattern for the very reason that we did not observe it in our experiments with polarized light. Although the transition between various degrees of polarization can alter the relative intensities of individual patterns, we do not expect these changes to be large enough to warrant a dramatic rise in the signal corresponding to the in-plane field components.

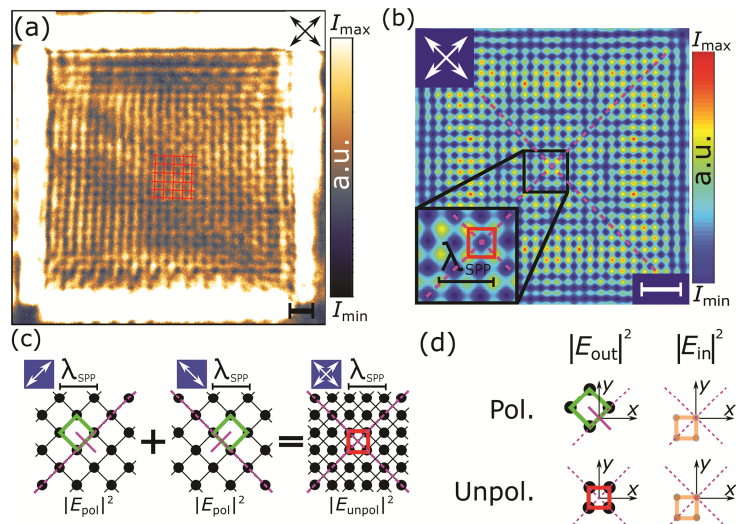


Fig. 6. (a) Experimental and (b) calculated interference patterns for unpolarized illumination at $\lambda = 650$ nm. The four-fold symmetry of the square-like pattern is indicated by the dashed purple lines. Scale bars are $1 \mu\text{m}$. (c) The observed square-like pattern is the result of incoherent superposition of two mutually shifted diamond-like patterns corresponding to two mutually perpendicular polarization states of incident light. (d) The absolute position of various interference patterns (polarized vs. unpolarized illumination; E_{in} vs. E_{out} components) with respect to the center of the interference structure.

The absence of the in-plane component in our measurements does not prevent us from inspecting a hypothetical situation where it dominates the detected signal. Although the pattern shape will be identical, its absolute position with respect to the center of symmetry will be shifted by a quarter of λ_{SPP} wavelength [see Fig. 6(d)]. Therefore, it should be in principle possible to distinguish E_{in} from E_{out} even under the unpolarized illumination, provided one has experimental data with sufficient resolution and quality. The fact that the shape of E_{out} patterns depends on the symmetry of illumination (its polarization) is an

important finding which indicates a strong link between interference patterns and symmetry of the experimental setup. This has practical implications, as any perturbation that breaks the lateral symmetry of the experiment will possibly manifest itself as an apparent anisotropy in the sensitivity of the probe towards SPPs propagating in different directions. The symmetry breaking can have its origin, for example, in elliptical probe aperture, partial polarization, tilting of the sample with respect to the tip or presence of a material anisotropy (e.g. in optical fiber transmittance). Therefore, by correlating observed variations in the interference patterns with intentional symmetry-changing modifications of individual experimental parts, one could in principle reveal the source of aberrations in the measured data.

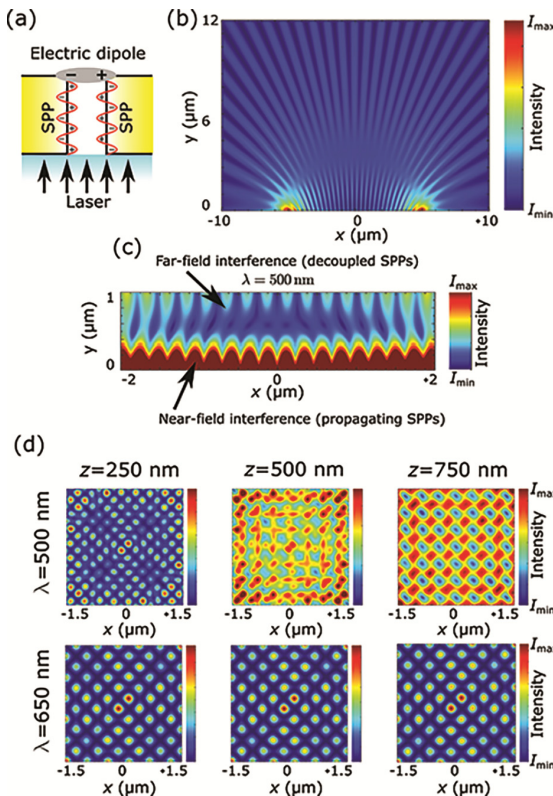


Fig. 7. (a) Schematic of the excitation of SPPs at the edges of the slit structure and their propagation through it. These SPPs are subsequently partially decoupled into free space radiation at the upper edge of the slits. This effect can be qualitatively modeled as an electric dipole radiation. (b) The corresponding far-field radiation interferes coherently and forms a distinct pattern with spatial periodicity larger than in the case of SPP interference. (c) Transition of the SPP near-field interference towards the far-field interference accompanied by the change in pattern periodicity. (d) Electric field maps ($|E|^2$) at different heights above the gold surface for two different wavelengths. For short wavelengths (below 550 nm), the pattern undergoes a transition from the near-field diamond-like to the far-field square-like character as we increase the distance from the surface. Although we performed our measurements with a conventional a-SNOM, thus with the tip-sample distance < 100 nm, the agreement between these simulations and experiment indicates that we also detect the free space radiation, probably through the probe sidewall: Despite the skin depth of gold below 550 nm is still significantly smaller (≈ 35 nm) than the probe coating (≈ 130 nm), the power flux through the sidewall, which was negligible at the longer wavelengths, can become comparable to the power transmitted through the aperture at these shorter wavelengths.

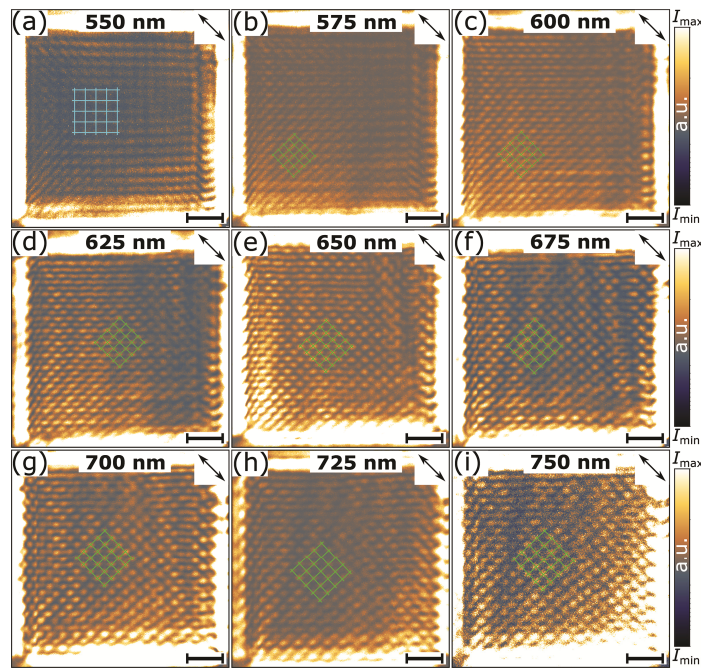


Fig. 8. Interference patterns measured for linearly polarized illumination at different wavelengths showing the same diamond-like pattern (indicated by the green grids) for all wavelengths ranging from 575 nm to 750 nm in agreement with the numerical simulations in Fig. 2. For shorter wavelengths the square-like pattern originating from the far-field interference of electromagnetic field decoupled from SPPs dominates (cyan grid). The scale bars are 2 μ m.

Once the interference patterns for a specific wavelength ($\lambda = 650$ nm) were measured and analyzed, we have proceeded to spectroscopic measurements for polarized illumination with wavelengths ranging from 500 nm to 750 nm. Below 550 nm, artefacts from an interference of electromagnetic far field decoupled from SPPs dominated in the SNOM images (see Fig. 7) [39,49] and, therefore, we have excluded them from further analysis. At all wavelengths above 550 nm, the SNOM images (see Fig. 8) exhibited diamond-like patterns, with values of λ_{SPP} in a good agreement with the theoretical ones [Fig. 9(a)] [38]. This observation renders the aforementioned domination of the out-of-plane component a more general and not spectrally-isolated phenomenon. Apart from the pattern periodicity, the theoretical calculations also revealed additional interesting aspects of SPPs patterns: First, the overall intensity of patterns rises with the illumination wavelength, indicating more efficient excitation of SPPs via the slits in the gold [50]. Second, the analytical description of a single propagating SPP predicts that as the illumination wavelength grows, the out-of-plane component of the electric field becomes increasingly dominant over the in-plane one [38]. In the case of (non-propagating) SPP interference patterns, this ratio further depends on how the individual SPPs constituting the pattern interfere with each other (see Fig. 4). Note that as the patterns corresponding to these two components are mutually shifted, it is more reasonable to compare their maximal values rather than the values at one specific point. We plot the analytically calculated ratio of $|E_{\text{out}}|^2$ and $|E_{\text{in}}|^2$ at respective interference maxima in Fig. 9(b), where the rapidly growing strength of the out-of-plane component with the increasing wavelength (up to the ratio in the order of 10^2 in the near infrared spectral region) can be observed. This effect, however, did not manifest itself in our spectroscopic measurements, probably due to substantially larger sensitivity of our setup towards the out-of-plane component, as discussed above. To eliminate the possibility that the in-plane pattern is actually present but obscured by its stronger diamond-like counterpart, we attempted to

locate the pattern in the reciprocal space (i.e. in Fourier-transformed images). Unfortunately, the FFT representations of the two patterns partially overlap, which makes their discrimination impossible unless very precise and quantitative measurements are carried out. So although we were not able to experimentally verify the behavior displayed in Fig. 9(b), it can be potentially valuable for future analyses of SNOM tip sensitivity: As the SNOM probes sensitive to either in- or out-of-plane components have been described in literature, we anticipate that by tuning the probe's parameters, one could achieve a state where the two field components contribute to the detected signal equally. Then simply by changing the illumination wavelength one should observe in the detected SNOM image a smooth transition between the two different pattern shapes. This would represent an unambiguous proof that a single SNOM probe can indeed detect the two components simultaneously.

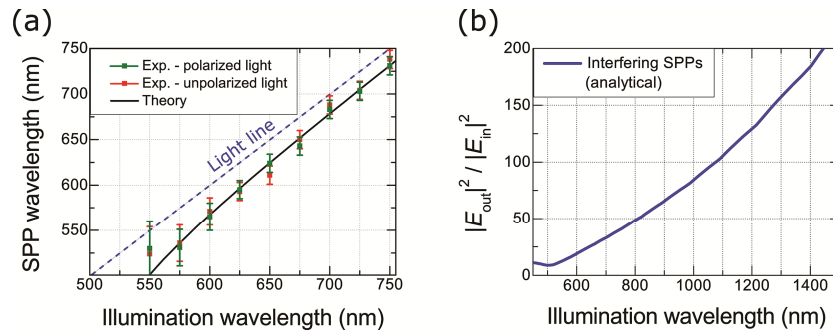


Fig. 9. (a) SPP wavelengths determined by an image analysis of patterns measured for polarized (green symbols) and unpolarized (red symbols) illumination and analytically calculated SPP wavelengths (black line) as a function of the illumination light wavelength. Note that at shorter wavelengths, the error bars are much longer because the peaks corresponding to the pattern periodicity are gradually approaching the central maximum of the Fourier images and thus becoming less and less resolvable. (b) Ratio of the maximal values of $|E_{out}|^2$ and $|E_{in}|^2$ for analytically calculated interfering SPPs at the air-gold interface as a function of the illumination wavelength.

In contrast to the spectroscopic experiments with polarized light, the unpolarized illumination gave us more complex results: As presented in Fig. 10, the measured interference patterns undergo a change in their character with increasing illumination wavelength. Below 550 nm, the patterns are again obscured by the far-field interference of electromagnetic field decoupled from SPPs [indicated by the large cyan squares in Figs. 10(a) and 10(b)]. For longer wavelengths, the square-like pattern can be observed [indicated by the red squares in Figs. 10(c)-9(f)], in accordance with the aforementioned formation mechanism [recall Fig. 6(c)]. The λ_{SPP} derived from these patterns, plotted in Fig. 8(a), scales with the illumination wavelength as predicted by the theoretical model of SPPs. In many randomly distributed areas in Figs. 10(b)-10(f), the diamond-like pattern appears as well (marked by the green diamonds). In the discussion above, we have shown that the diamond- and square-like patterns are related to polarized and unpolarized illumination, respectively [cf. Figure 6(d)]. Therefore, a natural explanation for appearance of the diamond-like patterns in Figs. 9(b)-9(f) can be a non-zero degree of polarization (DoP) of illuminating light [see schematics in Fig. 11(a)]. To verify this hypothesis, we measured the DoP of incoming light, obtaining nonzero values up to 0.3 at some wavelengths [Fig. 11(b)]. Simulations with various DoP then revealed that the mixture of diamond-like and square-like patterns emerges already for values around 0.2 [Fig. 11(c) and 11(d)], thus providing a solid explanation for the observed images. Although other symmetry-breaking perturbations and anisotropies do not seem to play a role in our case, they might have significant influence in other experimental configurations, manifesting themselves as pattern distortions. This makes

interference structures a useful tool for detection and elimination of such aberrations in SNOM experiments.

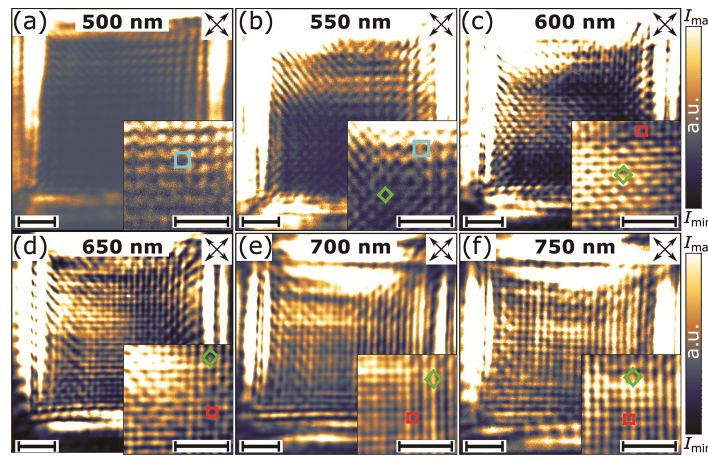


Fig. 10. Interference patterns measured at different wavelengths using unpolarized illumination. Nearly at all wavelengths a mixture of diamond-like (green) and square-like (red) patterns was observed. As we go towards shorter wavelengths (below 550 nm), a square-like pattern originating from the far-field interference of electromagnetic field decoupled from SPPs (cyan) starts to emerge and eventually dominates the entire image. All scale bars are 2 μm .

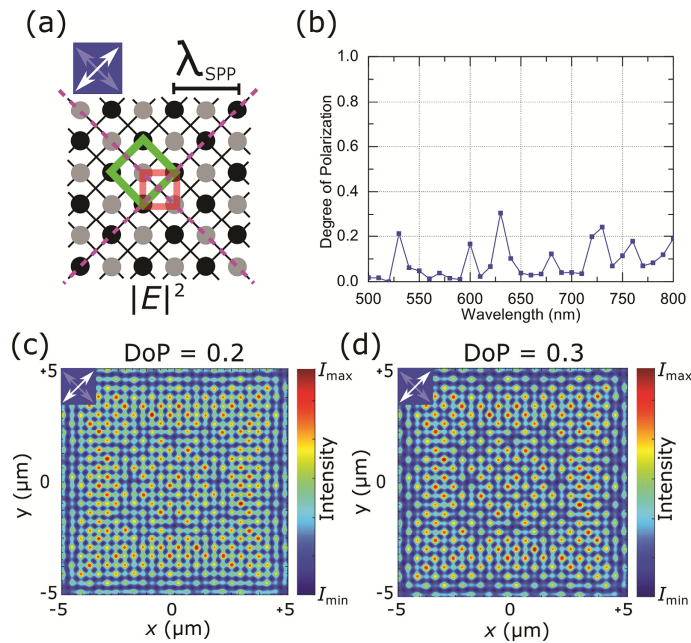


Fig. 11. (a) Formation of the interference pattern for partially polarized light. The breaking of the symmetry results in appearance of the diamond-like pattern on top of the originally square-like pattern. (b) Measured degree of polarization (DoP) of the used laser beam as a function of illumination wavelength. Simulated interference patterns at $\lambda = 650$ nm for a degree of polarization set to 0.2 (c) and 0.3 (d).

3. Conclusion

In summary, we used a spectroscopic a-SNOM setup for investigation of SPP interference patterns formed amongst four slits milled in a gold layer. Our results revealed a major

difference between the interference patterns formed under polarized and unpolarized illumination, i.e. their respective diamond-like and square-like characters. With the aid of FDTD simulations, we were able to clarify the mechanism of their formation, more specifically, the role of individual SPP field components. This allowed us to formulate two important conclusions regarding the near-field detection by a-SNOM: (1) The inherently larger out-of-plane electric field component dominates in our SNOM images at all relevant illumination wavelengths, regardless of the polarization state. In the context of reports from other research groups, this finding is rather unusual and challenges the widespread notion that this out-of-plane component does not couple to the a-SNOM probe. (2) The two patterns corresponding to the in-plane and out-of-plane components of SPP field are mutually shifted. This aspect of SPPs could find its use in assessment of SNOM probe sensitivity to these near-field components, which would be an important step towards full vector a-SNOM mapping. In addition, based on the results of our numerical simulation, we argue that there is a strong link between the shape of observed patterns and imperfections present in the experimental setup. This interconnection can be, in principle, also utilized for detection and elimination of such imperfections.

Funding

Grant Agency of the Czech Republic (grants No. 15-21581S and 15-14612S); MEYS CR [projects No. LQ1601 (CEITEC 2020) and LM2015041], Technology Agency of the Czech Republic (grant No. TE01020233) and BUT (project No. FSI/STI-J-15-2897).

Acknowledgment

We acknowledge CEITEC Nano Research Infrastructure for providing us with access to their facilities.